Multiplexed aberration measurement for deep tissue imaging *in vivo*

Chen Wang[1,2,4], Rui Liu[1,4], Daniel E Milkie[3,4], Wenzhi Sun[1], Zhongchao Tan[1], Aaron Kerlin[1], Tsai-Wen Chen[1], Douglas S Kim[1] & Na Ji[1]

We describe an adaptive optics method that modulates the intensity or phase of light rays at multiple pupil segments in parallel to determine the sample-induced aberration. Applicable to fluorescent protein–labeled structures of arbitrary complexity, it allowed us to obtain diffraction-limited resolution in various samples *in vivo*. For the strongly scattering mouse brain, a single aberration correction improved structural and functional imaging of fine neuronal processes over a large imaging volume.

Tissue refractive-index heterogeneity limits the imaging quality of two-photon fluorescence microscopy *in vivo* by distorting its excitation wavefront and resulting in an enlarged focal volume and reduced focal intensity. For imaging fine structures at depth, it is essential to measure and correct these sample-induced aberrations through adaptive optics (AO)[1]. An ideal aberration-measurement method should work with signal from structures intrinsic to the sample, under any labeling density, with any labeling strategy (from bright synthetic dye to dim fluorescent proteins), in any sample (from transparent to strongly scattering), and, if the sample permits, generate a corrective pattern that improves image quality over a large volume. Here we describe a multiplexed aberration-measurement method that satisfies all of the above criteria.

For a perfect focus, all light rays have to intersect at the same point and interfere with the same phase. Aberration modifies the directions and phases of these rays, which can be measured to obtain the corrective wavefront needed for restoring diffraction-limited focus. Consider the wavefront of an excitation beam illuminating the back pupil of a microscope objective: if we apply local phase ramps to a spatial light modulator (SLM) to raster scan the ray at one pupil segment while keeping all other rays fixed as reference, the varying interference between them modulates the focal intensity and, consequently, signal strength. Plotting the signal relative to the displacement of the ray in the focal plane as a two-dimensional (2D) signal-versus-displacement map, we can determine the local wavefront tilt for this particular ray by measuring the extra phase ramp needed to generate maximal interference[2]. Repeating the procedure for all light rays (**Fig. 1a**), we get the local wavefront gradients, from which the entire corrective wavefront can be obtained and applied to the SLM for aberration correction[3,4]. This method, using the fluorescence signal directly (the 'direct-signal' (DS) method), however, is slow: the interference between rays at a small pupil segment and the rest leads to only small signal variations (~1–2% for edge segments in **Fig. 1a**), whose detection requires long integration time; sequential measurement of each ray further increases the time needed. An aberration measurement using a moderate number (for example, 36 in **Fig. 1a**) of pupil segments may take longer than 20 min, making it impractical for *in vivo* applications because of sample photobleaching and motion. To speed up the process, we measure rays at multiple pupil segments in parallel through multiplexing[5]: tagging each ray with a characteristic frequency ω by modulating either its intensity or phase using a digital micromirror device (DMD) or a segmented deformable mirror (SDM) conjugated to the SLM (**Supplementary Fig. 1**), we separate the contribution of each ray in the final interference signal by Fourier-transforming the signal trace and plotting the Fourier magnitude for each ray at its distinct modulation frequency ω in the 2D map (**Fig. 1b** (intensity modulation with DMD), **Supplementary Fig. 2** and Online Methods). Besides speeding up the aberration measurement (by 18× in **Fig. 1b**; see **Supplementary Table 1** for measurement time and laser power), moving the measurement away from the direct signal also led to better signal-to-noise ratio because noise such as that associated with excitation power fluctuations is much smaller at higher frequency, thereby resulting in a better corrective performance (**Fig. 1c**,**d**). This multiplexed aberration-measurement method works in both sparsely and densely labeled samples and allowed us to correct sample-induced aberration using fluorescent protein signal from *Caenorhabditis elegans*, zebrafish larva and mouse brain *in vivo* (**Fig. 2**, **Supplementary Figs. 3** and **4** and **Supplementary Note**).

At layer 2/3 in the primary visual cortex of a mouse transfected with the genetically encoded calcium sensor GCaMP6s[6], a single corrective wavefront (**Fig. 2c**) obtained at the cell body (**Fig. 2a**, intensity modulation with DMD) improved both the signal and resolution of layer 2/3 neurons, with many more fine neuronal processes resolvable after AO correction (**Fig. 2a**,**b**). High label density led to a diffuse fluorescence background, which made it difficult to find isolated structures to quantify the signal improvement before and after AO, but the line intensity profile comparisons show that many previously invisible neuronal processes were

[1]Janelia Farm Research Campus, Howard Hughes Medical Institute, Ashburn, Virginia, USA. [2]State Key Laboratory of High Field Laser Physics, Shanghai Institute of Optics and Fine Mechanics, Chinese Academy of Sciences, Shanghai, China. [3]Coleman Technologies, Inc., Newtown Square, Pennsylvania, USA. [4]These authors contributed equally to this work. Correspondence should be addressed to N.J. (jin@janelia.hhmi.org).

RECEIVED 21 APRIL; ACCEPTED 27 JUNE; PUBLISHED ONLINE 17 AUGUST 2014; DOI:10.1038/NMETH.3068

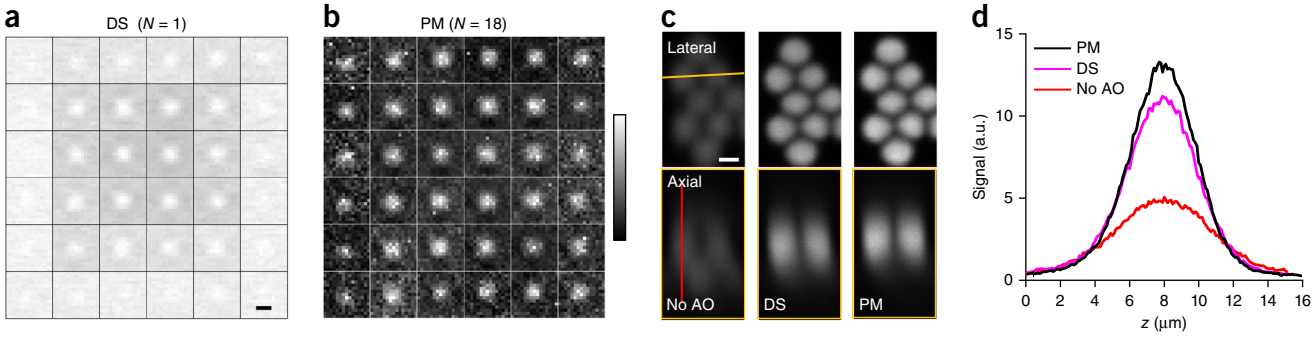

Figure 1 | Multiplexed aberration measurement with parallel modulation (PM) of light ray intensity at multiple pupil segments. (**a**,**b**) Signal-versus-displacement maps for 36 pupil segments obtained from the fluorescence signal directly (DS (N = 1)) (**a**) and from the Fourier magnitudes (PM (N = 18); 18 pupil segments modulated simultaneously with a DMD) (**b**). Each map is normalized between 0 and its maximum. (**c**) Lateral and axial (along the yellow line) images of 2-μm-diameter beads obtained without AO (left), with the corrective wavefront from the DS method (center) and with the corrective wavefront from the multiplexed method (right). (**d**) Signal profiles along the red line in **c**. Scale bars, 2 μm. a.u., arbitrary units. Signal intensity scales in **Figures 1**–**3** range from high (light) to low (dark).

easily detectable after AO correction (**Fig. 2b**). In contrast, the fluorescence background signal changed little because whereas the signal from smaller features is improved owing to the higher excitation intensity of an AO-corrected focus, an aberrated and enlarged focus can compensate for the loss of focal intensity by exciting more fluorophores in spatially extended structures[7]. This has important implications for *in vivo* calcium imaging experiments, in which the detected fluorescence change caused by neural activity may come from two sources: the individual neuronal structure of interest (for example, soma, axons and dendrites) and its surrounding, diffusely stained neuropil, with the latter signal often uncorrelated with stimulus feature and

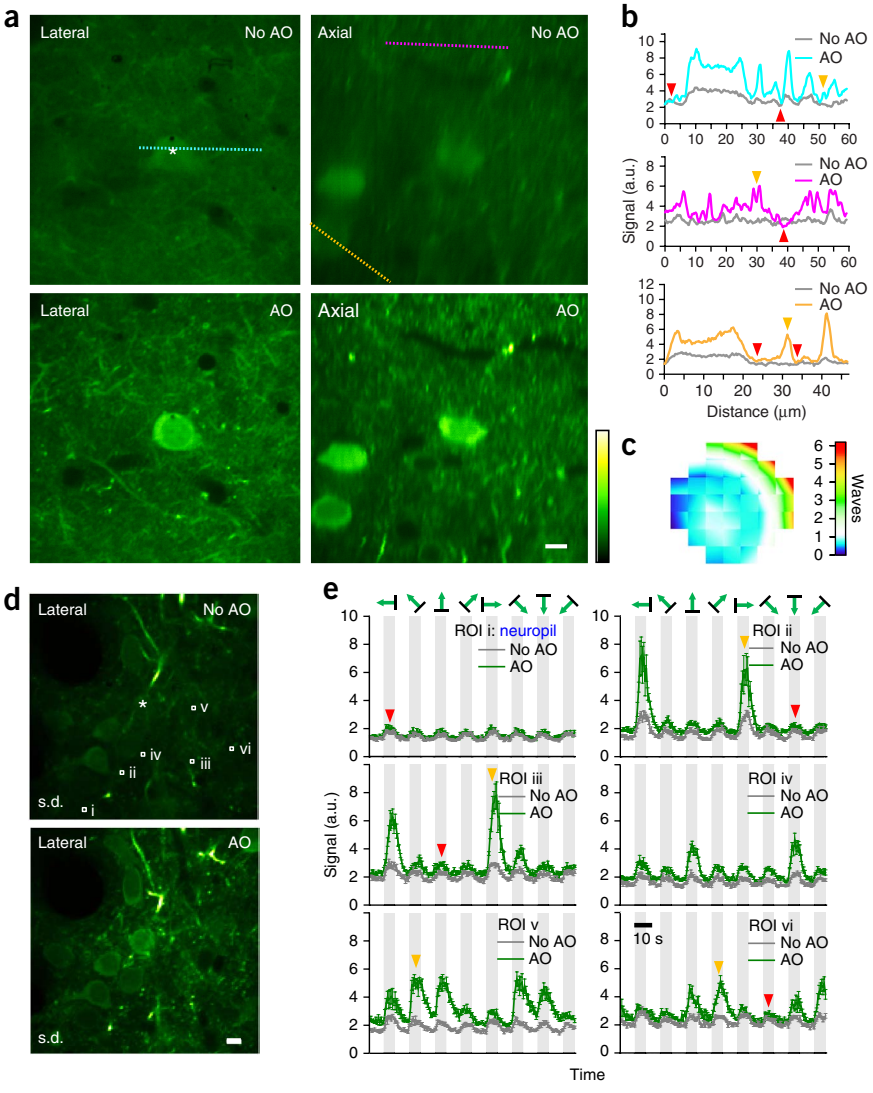

Figure 2 | AO correction with multiplexed aberration measurement at layer 2/3 of a GCaMP6s-expressing mouse brain *in vivo*. (**a**) Lateral and axial images at 115 μm below dura without and with AO correction (representative images of 33 experiments from 10 mice). (**b**) Signal profiles along the cyan, purple and orange lines in **a**. Orange arrowheads label the structures rendered invisible by the diffusely labeled background (red arrowheads). (**c**) Corrective wavefront in units of waves. (**d**) Lateral images at 150-μm depth without and with AO correction (representative images of 18 experiments from 10 mice). Pixel brightness reflects the s.d. of pixel values across 800 calcium imaging frames, with larger s.d. values indicating higher neuronal activity. (**e**) Fluorescence signals reflecting calcium transients measured without and with AO correction at six regions of interest (ROIs; white squares i–vi in **d**) under visual stimulations of gratings moving in eight different directions. Orange arrowheads mark the example responses at the preferred directions of grating motion; red arrowheads label example responses dominated by neuropil contamination. Gray bars denote the duration with stimuli on. Signals are averages of 5 trials of calcium imaging with the error bars indicating the s.e.m. Signals at the asterisks were used to measure aberration through multiplexed intensity modulation via DMD. "Green hot" lookup table in ImageJ is used for all images. Scale bars, 10 μm. a.u., arbitrary units.

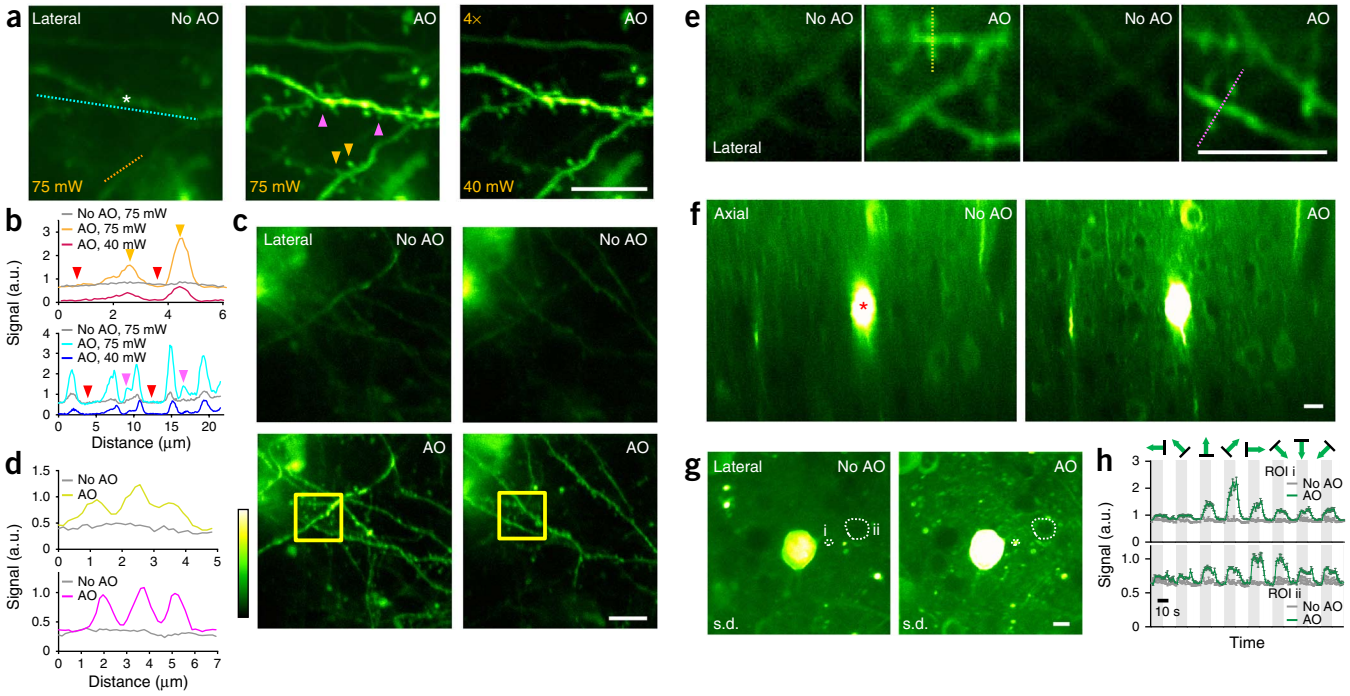

Figure 3 | AO correction with multiplexed aberration measurement at layers 4 and 5 of the mouse brain *in vivo*. (**a**) Maximal-intensity projections of dendrites at 376–395 μm below dura measured without and with AO at excitation powers 75 mW and 40 mW, respectively. The gain of the image taken at 40 mW is increased 4×. (**b**) Line intensity profiles along the orange and cyan lines in **a**. Purple and orange arrowheads label dendritic spines invisible before AO correction. Red arrowheads indicate the out-of-focus background level at 75-mW excitation. (**c**) Maximal-intensity projections of basal dendrites at 473–481 μm (left) and 481–490 μm (right) measured without and with AO correction. (**d**) Line intensity profiles along the yellow and violet lines in **e**. (**e**) Images taken inside the yellow squares in **c** at 480-μm (left) and 484-μm (right) depths without and with AO correction. (**f**) Axial images at 427- to 547-μm depth measured without and with AO. (**g**) From **f**, lateral images at 490-μm depth without and with AO correction. Pixel brightness reflects the s.d. of pixel values across 800 calcium imaging frames. (**h**) Calcium transients as in **Figure 2e** measured without and with AO correction at the two regions of interest in **g** (ROI i, dendrite; ROI ii, soma). Signals are averages of 5 trials of calcium imaging with the error bars indicating the s.e.m. In **a**,**f**, corrective wavefront was measured at the asterisk; in **c**, correction was at 30 μm above the imaging volume. In **a**,**c**, phase modulation with SDM was performed; **f**, intensity modulation with SDM. For **a**–**e**, thy1-YFP-H mice were used (representative images of 12 experiments from 10 mice); **f**–**h**, wild-type mouse expressing GCaMP6s (representative images of 5 experiments from 5 mice). "Green hot" lookup table in ImageJ is used for all images. Scale bars, 10 μm. a.u., arbitrary units.

considered a contamination[8]. With AO improving the strength of the desired signal much more than neuropil contamination (**Fig. 2e**), more calcium events could be detected (**Fig. 2d** and **Supplementary Video 1**), and, with the increase of signal-to-neuropil ratio, the orientation selectivity of dendrites could be determined with confidence (**Fig. 2e**).

With increasing imaging depth, the excitation laser power had to be increased to compensate for the scattering loss of ballistic photons at the focus. Eventually, the laser intensity at the surface of the brain was high enough to excite superficially labeled structures without requiring the spatial confinement of a focus, resulting in a background signal in even sparsely labeled brains (**Fig. 3a**; post-objective power at 75 mW, at 385-μm depth inside a thy1-YFP-H mouse brain), which would ultimately overwhelm the signal generated at the focus and limit the imaging depth[9]. This out-of-focus signal is not affected by the presence of aberration[10] and was therefore not increased by AO correction (**Fig. 3b**). The in-focus signal, however, strongly depends on the focus quality. After AO correction (phase modulation with SDM), dendritic spines previously rendered invisible by the background in the uncorrected image became clearly visible (**Fig. 3a**,**b**). The improvement in both resolution and signal allowed us to reduce excitation power (for example, from 75 mW to 40 mW) yet still obtain a higher quality image with much-suppressed out-of-focus background.

With the synaptic-level resolution provided by AO, we could resolve the submicrometer-sized spines on the basal dendrites of layer 5 pyramidal neurons at depth. Without AO correction, at 458- to 500-μm depth, only the crude profiles of these dendrites could be detected. AO correction elevated the signal from dendritic spines to rise above background noise, making them easily identifiable in the corrected images (**Fig. 3c–e** and **Supplementary Videos 2** and **3**; thy1-YFP-H mouse, phase modulation with SDM). For more densely labeled brain, fine neuronal processes and even the much larger somata went from invisible to clearly resolvable after AO correction (**Fig. 3f**; 427- to 547-μm depth, wild-type mouse with GCaMP6s expression, intensity modulation with SDM), in which the nuclei of neurons appeared dark owing to the nucleus exclusion of GCaMP6s in healthy neurons. Finally, AO drastically improved calcium imaging of fine neuronal processes and somata at depth: at 490-μm depth, structures whose calcium activity were undetectable without aberration correction showed clear visually evoked calcium transients after correction (**Fig. 3g**,**h** and **Supplementary Video 4**).

Besides aberration, light scattering by minuscule scatterers such as cellular organelles also limits image quality *in vivo*. These much

higher spatial-frequency wavefront perturbations may be partially corrected via wavefront shaping[11,12]. However, because the tissue scattering profile is highly spatially variable, a corrective pattern improves signal in only a small volume (for example, $6 \times 6 \times 7\ \mu m^3$ in fixed brain tissues[13]). In contrast, because aberration correction removes the lower-order wavefront errors, in the case of mouse brain *in vivo*, one correction pattern improves signal over a much larger volume (for example, $168 \times 168 \times 120\ \mu m^3$ in **Fig. 3f**). Furthermore, for all the *in vivo* samples tested by us, optical aberration was temporally stable over the experimental duration (for example, data in **Fig. 3g**,**h** was obtained 3 h after aberration measurement). In comparison, because of its susceptibility to microscopic motions, the tissue scattering profile may vary rapidly in time[14]. Therefore, for applications requiring a large field of view and an extended imaging period, correcting optical aberration may be a more generally applicable approach for deep tissue imaging.

With current wavefront-shaping hardware and fluorescent protein brightness, we obtain a corrective wavefront within minutes. Although it is still slow compared to direct wavefront-sensing methods[15], which work only in transparent samples, our method is applicable to strongly scattering tissues. Because, in mouse brain, a single correction improves ensuing experiments for hours, the extra time required for aberration measurement does not constitute a substantial burden while allowing us to image the major input and output layers of mouse cortex *in vivo* with synaptic-level resolution.

METHODS

Methods and any associated references are available in the online version of the paper.

Note: Any Supplementary Information and Source Data files are available in the online version of the paper.

ACKNOWLEDGMENTS

We thank our colleagues at Janelia Farm Research Campus, Howard Hughes Medical Institute: E. Betzig for helpful discussions; H. Dana, B. MacLennan, G. Ranganathan, K. Smith for help with mice samples; and P. Keller and M. Ahrens for providing zebrafish samples. We thank C. Fang-Yen for advice on *C. elegans* samples. This work was supported by Howard Hughes Medical Institute.

AUTHOR CONTRIBUTIONS

N.J. conceived of the project and designed the experiments; C.W., R.L. and N.J. designed and built the optical setup; D.E.M. and N.J. developed the instrument control program; C.W. and R.L. debugged the program; C.W. (intensity modulation with DMD and SDM, morphological and functional imaging), R.L. (phase and intensity modulation with SDM, spine morphological imaging) and N.J. performed the experiments and analyzed the data; W.S., Z.T., A.K. and R.L. prepared the mice for *in vivo* imaging; T.-W.C. and D.S.K. provided GCaMP6s reagents; and N.J. wrote the paper with input from all coauthors.

COMPETING FINANCIAL INTERESTS

The authors declare no competing financial interests.

1. Kubby, J.A. *Adaptive Optics for Biological Imaging* (CRC Press, 2013).
2. Milkie, D.E., Betzig, E. & Ji, N. *Opt. Lett.* **36**, 4206–4208 (2011).
3. Ji, N., Milkie, D.E. & Betzig, E. *Nat. Methods* **7**, 141–147 (2010).
4. Liu, R., Milkie, D.E., Kerlin, A., MacLennan, B. & Ji, N. *Opt. Express* **22**, 1619–1628 (2014).
5. Bridges, W.B. *et al. Appl. Opt.* **13**, 291–300 (1974).
6. Chen, T.-W. *et al. Nature* **499**, 295–300 (2013).
7. Ji, N., Sato, T.R. & Betzig, E. *Proc. Natl. Acad. Sci. USA* **109**, 22–27 (2012).
8. Göbel, W. & Helmchen, F. *Physiology (Bethesda)* **22**, 358–365 (2007).
9. Theer, P., Hasan, M.T. & Denk, W. *Opt. Lett.* **28**, 1022–1024 (2003).
10. Leray, A., Lillis, K. & Mertz, J. *Biophys. J.* **94**, 1449–1458 (2008).
11. Vellekoop, I.M. & Mosk, A.P. *Opt. Lett.* **32**, 2309–2311 (2007).
12. Yaqoob, Z., Psaltis, D., Feld, M.S. & Yang, C. *Nat. Photonics* **2**, 110–115 (2008).
13. Tang, J., Germain, R.N. & Cui, M. *Proc. Natl. Acad. Sci. USA* **109**, 8434–8439 (2012).
14. Cui, M., McDowell, E.J. & Yang, C. *Opt. Express* **18**, 25–30 (2010).
15. Wang, K. *et al. Nat. Methods* **11**, 625–628 (2014).

ONLINE METHODS

All experiments were performed according to methods approved by the Janelia Farm Institutional Animal Care and Use Committee.

Adaptive-optical two-photon fluorescence microscope. A simplified schematic of our microscope is shown (**Supplementary Fig. 1a**). Femtosecond pulses at 900 nm from a titanium-sapphire laser (Ti:Sapphire, Chameleon Ultra II, Coherent) are reflected off either a segmented deformable mirror (SDM, Iris AO) or a high-speed digital micromirror device (DMD,V4100, ViALUX Messtechnik+Bildverarbeitung) following a dispersion compensation unit (DCU). A pair of achromat doublets (AC300-080-B and AC254-500-B, Thorlabs) are used to conjugate the DMD or SDM to a liquid-crystal, phase-only spatial light modulator (SLM, PLUTO-NIR, Holoeye Photonics), which is further conjugated to a pair of galvanometers (X galvo and Y galvo, 3-mm beam aperture, 6215H, Cambridge Technology) and the back pupil plane of a 40× or a 16×, numerical aperture (NA) 0.8 water-dipping objective (CFI Apo 40XW NIR, CFI LWD 16XW, Nikon) using three pairs of achromat doublets (AC254-150-B and AC254-060-B, AC508-080-B and AC508-080-B, AC508-75-B and 014-1310, Thorlabs and OptoSigma). A field stop (FS) is located at the intermediate image plane between the DMD/SDM and the SLM to block unwanted diffraction orders. The microscope objective is mounted on a single-axis piezo stage (P-725.4CD, Physik Instrumente) for taking axial images. In the detection path, fluorescence signal reflected from a dichroic long-pass beam splitter (FF665-Di02-25x36, Semrock) immediately above the objective gets collected by a photomultiplier tube (PMT, H7422-40, Hamamatsu) after passing through an emission filter (FF01-680/SP, Semrock). Ray-tracing software Zemax (Zemax 12 EE, Radiant Zemax) is used to optimize the design of optical path. With the DMD, two SLM patterns are used for AO correction (i.e., two pupil-segmentation schemes) (**Supplementary Fig. 1d**), with the active area of the SLM inscribed to the back pupil. With SDM, the hexagon formed by 37 mirror segments is slightly larger than the back pupil.

Operation of the DMD and the SDM. The DMD is a bistable spatial light modulator capable of intensity modulation, consisting of 1,024 × 768 movable micromirrors, where each mirror can be individually deflected at ±12° about a hinged diagonal axis. We rotate the DMD by 45° around its surface normal so that the diagonal axes are parallel to the optical table, simplifying the direction and polarization control for the deflected light. The DMD is then divided into segments through precision mapping to the SLM segments. The DMD is capable of a maximum binary switching rate of 22,727 Hz, but to generate a variety of modulation frequencies for different pupil segments, we utilize pulse-width modulation to have grayscale control for each DMD segment. Throughout this study, we operated the DMD at a bit depth of 5, which provides 32 gray levels and a switching rate of 2,016 Hz. We chose the signal integration time at each gray level to be the reverse of the switching rate (0.5 ms) so that the resulting fluorescence signal reflects the gray-level value.

Optically, the DMD acts as a blazed grating; thus, the coherent light from the Ti:Sapphire laser bouncing off the DMD travels along discrete directions dictated by diffraction. We adjust the incident angle of the laser beam to maximize the energy in the brightest diffraction order, achieving 30% diffraction efficiency at 900 nm. A further complication arises because femtosecond pulses are not monochromatic and thus are spatially dispersed by the DMD in the incidence plane at ~0.026°/nm around 900 nm. Without compensation, the angular spread of the different frequency components leads to a focus elongated in the direction of dispersion (**Supplementary Fig. 1c**). For dispersion compensation, we built a dispersion compensation unit (DCU) based on a single-prism approach[16,17] (**Supplementary Fig. 1b**). An equilateral dispersive prism (EDP, PS855, Thorlabs) with an incident angle of 49.3° was used for dispersion compensation. To counter the 1D demagnification the beam experienced while traveling through the EDP, we used an anamorphic prism pair (APP, NT47-244, Edmund Optics) to expand the beam ~5× in the same dimension. The lateral image profiles of 2-µm beads became much more circular after dispersion compensation (**Supplementary Fig. 1c**).

The SDM is made of piston-tip-tilt mirror segments and operated in two modes: by modulating the piston value of each mirror segment, we modulate the phase of the light ray at the corresponding pupil segment; by tilting each mirror segment so that the reflected ray gets blocked by the field stop, we modulate the light intensity at its pupil segment. Both types of modulation affect the interference between the light ray and the reference focus. Without the need for dispersion compensation, the SDM provides better power throughput. It also has the potential to replace the SLM for aberration correction and could thus simplify the setup substantially. However, once the magnification between the SDM and the SLM is determined, the number of pupil segments is fixed at 37 in our experiment, whereas the DMD, with vastly more independent actuators, allows us to vary the number of pupil segments.

Multiplexed aberration-measurement method. For half of all pupil segments, we applied a phase ramp R_{ikjk} to pupil segment k via the SLM ((1) in **Supplementary Fig. 2**). For each pupil segment, the phase ramp R_{ikjk} was randomly chosen from a set of total N_R phase ramps, which together led to a 2D grid displacement of the deflected ray in the focal plane around its original location ($R_{ij} = 0$). This way, we prevented the modulated light rays from landing at the same location in the focal plane and forming a focus of similar intensity to that of the reference focus, which would interfere with the reference focus at near-zero displacements and lead to spurious signal near the center of the final maps. Using the DMD or SDM, we modulated the illumination intensity or phase of rays impinging on these pupil segments at distinct frequency ω_k for time duration T while monitoring the signal change. The amount of interference that each pupil segment had with the reference focus was found by reading out the magnitude M_{ikjk} at its distinct modulation frequency ω_k from the Fourier transform of the signal trace (inspired by the multidither coherent optical adaptive technique[5], although in our implementation we read out the magnitudes rather than the phases).

Repeating (1) N_R times, the whole set of phase ramps was applied each segment, and the resulting Fourier magnitudes M_{ij} were measured. Signal-versus-displacement maps were then formed for these modulated pupil segments by plotting the magnitude M_{ij} values according to the displacements of the rays in the focal plane ((2) in **Supplementary Fig. 2**). The wavefront tilt

for each particular pupil segment could then be measured from the shift of the peak from the center, just as in a Shack-Hartmann wavefront sensor[18]. Whereas a peak modulation magnitude always exists for phase modulation, for intensity modulation, if there is a ~90° phase shift between the ray and the reference focus, a clear maximum would be absent from the resulting map; a 90° phase offset was then added to the corresponding local wavefront and the measurement repeated.

Repeating (2) one more time for the other half of the pupil segments, we obtained the local wavefront gradients for all pupil segments ((3) in **Supplementary Fig. 2**), with an overall signal integration time of $2 \times N_R \times T$. Next, by applying either phase reconstruction algorithms or phase measurement methods[4], we obtained the corrective wavefront. Depending on the sample, N_R varied between 100 and 256 (10 × 10 to 16 × 16 2D grid), and T varied between 45 and 360 ms (and could be smaller if higher signal level was used). Additional overheads due to the hardware (for example, SLM update time) and software (for example, time to calculate DMD and SLM patterns) usually increased the overall correction time by 50%. For large initial aberrations, additional rounds of correction can improve the correction by having an increasingly aberration-free reference focus. For all biological samples shown in the paper, two or three rounds were used to obtain the final corrective wavefront.

Typical operational parameters. As an example, we describe here the detailed imaging parameters for the data shown in **Figure 1**. The same integration time per phase ramp (T = 180 ms) was used in all measurements. 15 × 15 phase ramps (N_R = 225) that displaced rays by ±15 µm in x and y directions in the focal plane were applied. With 6 × 6 pupil segments, (N_P = 36), the serial method (i.e., the DS method with overall integration time of $N_P \times N_R \times T$) had an overall integration time of 1,458 s or 24 min (and an overall correction time of 3,568 s), whereas the multiplexed method had an overall integration time of 81 s (and an overall correction time of 127 s).

System aberration was corrected before all measurements, and the resulting diffraction-limited microscope was used to take all data labeled with "No AO." Experimentally, we parked the laser focus at one sample location and used the fluorescence signal from this location for AO correction. (More generally, we can scan the laser focus across a user-defined area or volume and use the integrated signal for AO correction. This will lead to an AO correction that is applicable to a large area/volume of the sample but would slow down the correction speed because of longer scanning time.) Because full-pupil illumination was used, no extra excitation power increase was needed during AO correction. Depending on the samples, the excitation power post objective varied from 0.2 mW (fluorescent beads), 9.1 mW (layer 2/3 in mouse cortex), to 75 mW (layer 5 in mouse cortex). For all *in vivo* samples, care was taken to make sure that no observable photobleaching or photodamage occurred. For mouse, images were often collected from the same mouse over multiple days at similar excitation power, and no obvious photoinduced morphological changes were observed. **Supplementary Table 1** lists the excitation power and time used for different samples.

Comparison with the single-segment illumination method. The signal-versus-displacement maps presented in **Figure 1** reflect only the focal intensity variation relative to the ray displacement in focal plane and do not reflect or rely on specific fluorescent structures of the sample. Therefore, we can achieve AO correction from fluorescent samples of arbitrary structural complexity, including densely labeled *C. elegans* and zebrafish (**Supplementary Figs. 3** and **4** and **Supplementary Note**). The single-segment illumination method[3] fails in such samples (e.g., densely labeled mouse brain, **Supplementary Fig. 5**) because the reduction of excitation NA during single-segment illumination allows the originally out-of-focus fluorescent structures to appear in the image and makes it difficult to determine wavefront gradients[2]. In contrast, the multiplexed method works even in a fluorescent solution (**Supplementary Fig. 6** and **Supplementary Note**).

Functional imaging in the mouse brain *in vivo*. We transfected neurons in the mouse primary visual cortex with GCaMP6s and recorded the fluorescence signal variation when mice were shown visual stimulations composed of grating patterns moving in eight different directions. For all functional imaging data, each direction lasted for ten image frames separated by ten frames with no visual stimulation present (i.e., 160 frames for one round of calcium imaging). Five trials of measurement (i.e., 800 frames total) were repeated for each imaging condition ("AO" or "No AO") for all functional imaging sessions. The trial-averaged results are shown. All movies have their brightest pixels saturated to improve the visibility of structures with weaker signals.

Digital image processing. All images are presented with no digital manipulation except those listed below. Due to brain motion at depth during functional imaging, TurboReg plug-in in ImageJ was used for image registration. Images are presented using either the grayscale or the "Green hot" lookup table (to make the weaker feature more visible) in ImageJ. For images in which the signal was too weak before AO correction, a linear scaling factor was applied to all pixels to improve visibility with the scaling factor listed on the image. No deconvolution or nonlinear scaling such as gamma correction was used on the data.

Sample preparation. *Beads.* Carboxylate-modified fluorescent microspheres of 1-µm and 2-µm diameters (F-8821 and F-8826, Invitrogen) were immobilized on poly(l-lysine)-coated microscope slides (12-550-12, Fisher Scientific). Under our two-photon fluorescence microscope, they generate red fluorescence when excited at 900 nm.

C. elegans. *C. elegans* larvae of strain ST2, with GFP expressed in nearly all neurons, were used for all experiments. Before imaging, the worms were transferred to a 2% agar pad made with M9 buffer. 5 µL of 100 mM sodium azide were then added to anesthetize the worms before a no. 1.5 coverslip was gently laid over the worms. The worms stayed immobilized for 2–3 h during imaging.

Zebrafish larvae. Zebrafish (*Danio rerio)* embryos of Tg(β-actin: HRAS-EGFP) line were grown at 28 °C in E3 zebrafish embryo medium. Between 10 and 16 hours post fertilization (h.p.f.), the embryos were transferred into 1× phenylthiourea (PTU) solution in E3 medium to inhibit melanin formation and render the embryos optically transparent[19]. Before imaging, the chorions, if present, were manually removed using forceps under a

doi:10.1038/nmeth.3068

stereomicroscope. Four-day-old larvae were then anesthetized in E3 medium containing 1× tricaine and immobilized on a microscope slide by embedding them in 1% low–melting point agarose with 1× PTU and 1× tricaine. During imaging, E3 medium containing 1× PTU and 1× tricaine was used as immersion medium.

Mouse. Procedures for viral infection and craniotomy were described previously[7]. Briefly, wild-type mice (C57BL/6Crl) older than P60 of both sexes were anesthetized with isoflurane (2% vol isoflurane/vol O_2). Following a craniotomy, 20 nL of suspended AAV1-syn-GCaMP6s-WPRE-SV40 virus were slowly injected into the neocortex at 300 μm and 500 μm below dura below the pia of anesthetized adult mice. A cranial window made of one or two no. 1.5 coverslips was then gently placed over the craniotomy and sealed onto the skull with dental cement. 3–12 weeks after viral injection, mice were anesthetized and mounted under the AO two-photon microscope for imaging.

16. Zeng, S. *et al. Opt. Lett.* **31**, 1091–1093 (2006).
17. Grewe, B.F., Langer, D., Kasper, H., Kampa, B.M. & Helmchen, F. *Nat. Methods* **7**, 399–405 (2010).
18. Hardy, J.W. *Adaptive Optics for Astronomical Telescopes* (Oxford Univ. Press, 1998).
19. Godinho, L. *Cold Spring Harb. Protoc.* **2011**, 879–883 (2011).